NANO LETTERS

pubs.acs.org/NanoLett Letter

Quantum-Size-Effect Tuning Enables Narrowband IR Photodetection with Low Sunlight Interference

Joao M. Pina, Maral Vafaie, Darshan H. Parmar, Ozan Atan, Pan Xia, Yangning Zhang, Amin M. Najarian, F. Pelayo García de Arquer, Sjoerd Hoogland, and Edward H. Sargent*

Cite This: https://doi.org/10.1021/acs.nanolett.2c02756 Read Online

ACCESS | Metrics & More | Article Recommendations | Supporting Information

ABSTRACT: Infrared photodetection enables depth imaging techniques such as structured light and time-of-flight. Traditional photodetectors rely on silicon (Si); however, the bandgap of Si limits photodetection to wavelengths shorter than 1100 nm. Photodetector operation centered at 1370 nm benefits from lower sunlight interference due to atmospheric absorption. Here, we report 1370 nm-operating colloidal quantum dot (CQD) photodetectors and evaluate their outdoor performance. We develop a surface-ligand engineering strategy to tune the electronic properties of each CQD layer and fabricate photodetectors in an inverted (PIN) architecture. The strategy enables photodetectors with an external quantum efficiency of 75% and a low dark current (1 $\mu A/cm^2$). Outdoor testing demonstrates that CQD-based photodetectors combined with a 10 nm-line width bandpass filter centered at 1370 nm achieve over 2 orders of magnitude (140× at incident intensity 1 $\mu W/cm^2$) higher signal-to-background ratio than do Si-based photodetectors that use an analogous bandpass filter centered at 905 nm.

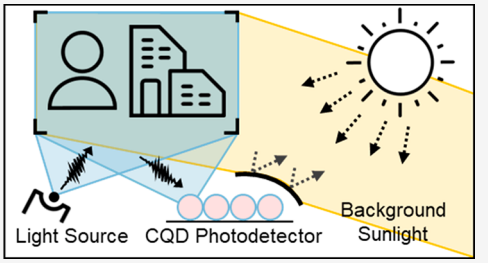

KEYWORDS: *depth imaging, time-of-flight, structured light, infrared, colloidal quantum dots, photodetectors*

Depth imaging techniques, such as structured light (SL) and time-of-flight (ToF), rely on infrared light pulses toward the object and the photodetection of the backscattered light (Figure 1a). Ambient illumination—in particular, sunlight—contributes to unwanted background current that degrades the accuracy and resolution of these techniques.[1−5] Depth imaging techniques, such as SL, require that the projected pattern's light intensity be comparable with that of the ambient light;[2] yet sunlight is often 2−5 orders of magnitude brighter than the projected infrared light,[1] making many depth imaging systems unsuitable for outdoor operation.[1−3] These systems commonly rely on silicon (Si) photodetectors due to their highly scaled, low-cost production. As the bandgap of Si limits photodetection to wavelengths shorter than 1100 nm, depth imaging systems operate with 850−950 nm light sources.[6,7]

Operation at longer wavelengths—in particular, centered at 1370 nm—benefits from low solar irradiance (Figure 1b). The vertical (earth-space) atmospheric attenuation caused by water vapor leads to low solar irradiance at 1370 nm.[8] However, the horizontal (sea-level) atmospheric attenuation is less impacted by water absorption. In clear sky conditions, water absorption does not degrade depth imaging meaningfully as the volume of water in the air is low, even in the case of elevated (100%) humidity.[9] This makes 1370 nm a promising wavelength for depth imaging applications for consumer electronics. Colloidal quantum dots (CQD) can be tuned to have a narrowband excitonic absorption peak at 1370 nm (Figure 1c). CQD are low-cost and readily integrated with read-out integrated circuits (ROICs).[10] The present-day alternatives to CQD, such as InGaAs and germanium (Ge), are costly from the viewpoint of consumer electronics applications.[10]

A CQD photodetector operating at 1370 nm can be combined with a bandpass filter to decrease photogeneration associated with solar background radiation. The solar radiation that transmits through the bandpass filter reaches the photodetector and produces an unwanted background current. Operating at 1370 nm has the potential of achieving 4 orders of magnitude lower background current than operation at 905 nm (Figure 1c and Note S1). Our analysis uses an idealized bandpass filter centered at 1370 nm, having 10 nm line width, 0 O.D. within the passband, perfect rejection outside of the passband, and projects a background current of 10^{-8} A/cm^2 because of the low solar background in this spectral band (Figure 1c and Note S1). In contrast, a photodetector using an analogous bandpass filter centered at 905 nm has a background current of 10^{-4} A/cm^2 (Figure 1c and Note S1), a consequence of the higher solar fluence in this spectral range. The improvement achieved at 1370 nm reduces the

Received: July 12, 2022
Revised: August 10, 2022

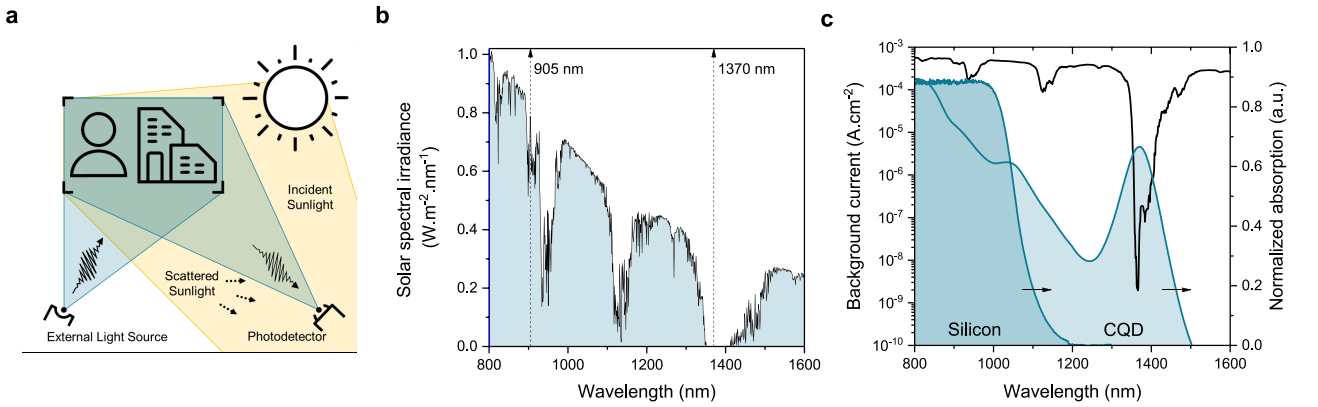

Figure 1. Decreased sunlight interference at 1370 nm. (a) Depth imaging techniques, such as SL and ToF. An external light source is used to image the object; in addition, though, the photodetector receives signal from incident and scattered sunlight. (b) Solar spectral irradiance. (c) Estimated background current produced by incident sunlight (calculated for a photodetector with an EQE of 80% with an ideal bandpass filter of 10 nm and assuming directly incident solar spectral irradiance) and normalized absorption of Si and CQD.

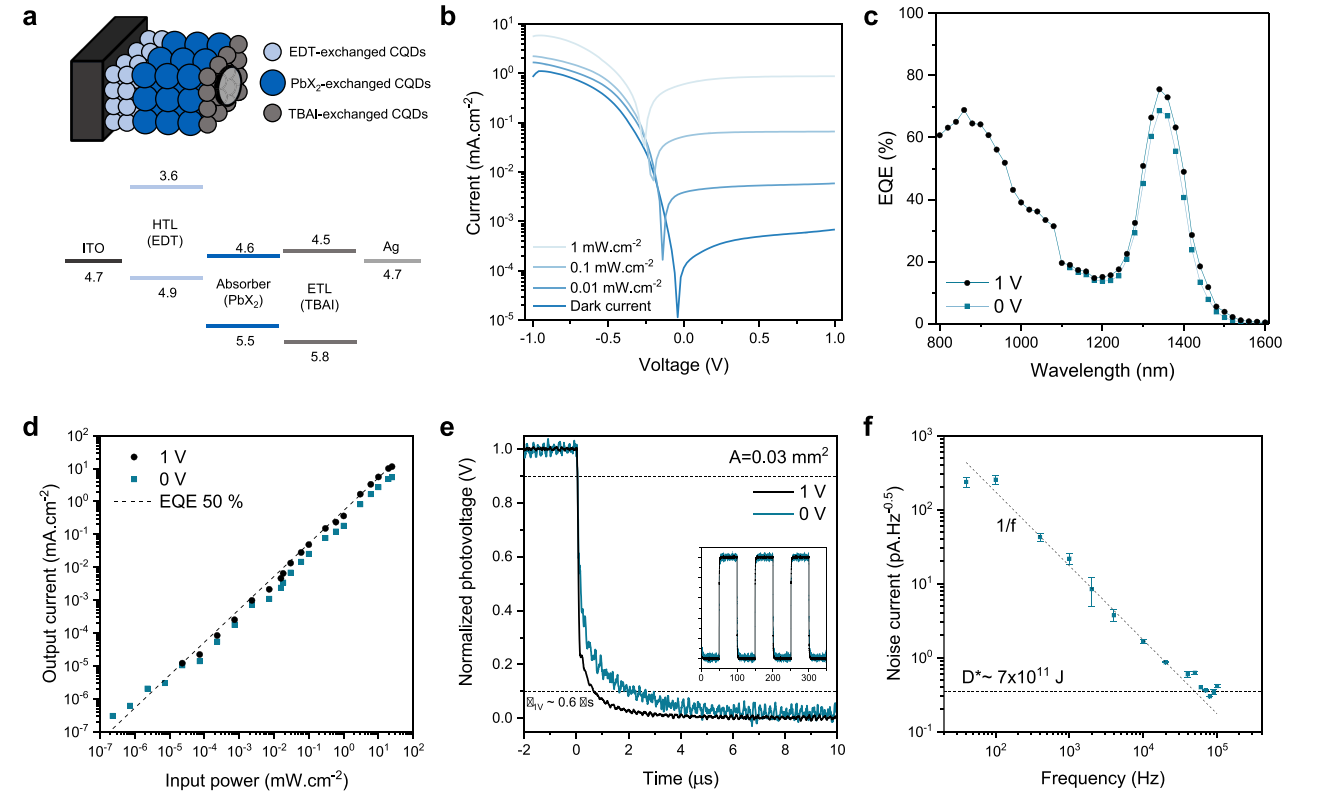

Figure 2. Performance of CQD photodetectors operating at 1370 nm. (a) Schematic and band diagram of the fabricated devices. (b) Current−voltage characteristics at various illumination intensities using 1310 nm laser excitation. (c) EQE spectrum. (d) Dynamic range using 1310 nm laser excitation. (e) Temporal response with cursors showing a fall-time of 600 ns. Inset shows three ON−OFF cycles. (f) Dependence of the noise current on the frequency at short-circuit conditions.

need for complex signal postprocessing and can be exploited to decrease power consumption.

Prior works have shown the potential of CQD materials for photodetector applications operating in the short-wave infrared (SWIR) spectral range (1300−2000 nm).[11−15] However, novel material and device fabrication strategies must be explored to achieve higher external quantum efficiencies (EQE) and lower dark currents. Inverted (PIN) structures−wherein the p-type hole transport layer (HTL) is in direct contact with the substrate−remain underexplored. An inverted design enables the use of novel transport layers, and it has been demonstrated to have advantages compared to the standard (NIP) architecture, such as decreased crosstalk and blooming in an ROIC.[16] Prior efforts have laid the foundations for the fabrication of inverted photodetectors,[17−19] but further efforts are needed to reach the performance of standard (not-inverted) structures.

Herein, we develop inverted CQD-based photodetectors operating at 1370 nm and demonstrate an improvement in EQE and dark current compared to prior literature in the SWIR. We compare the outdoor performance of these photodetectors operating at 1370 nm with commercial Si-

https://doi.org/10.1021/acs.nanolett.2c02756
Nano Lett. XXXX, XXX, XXX−XXX

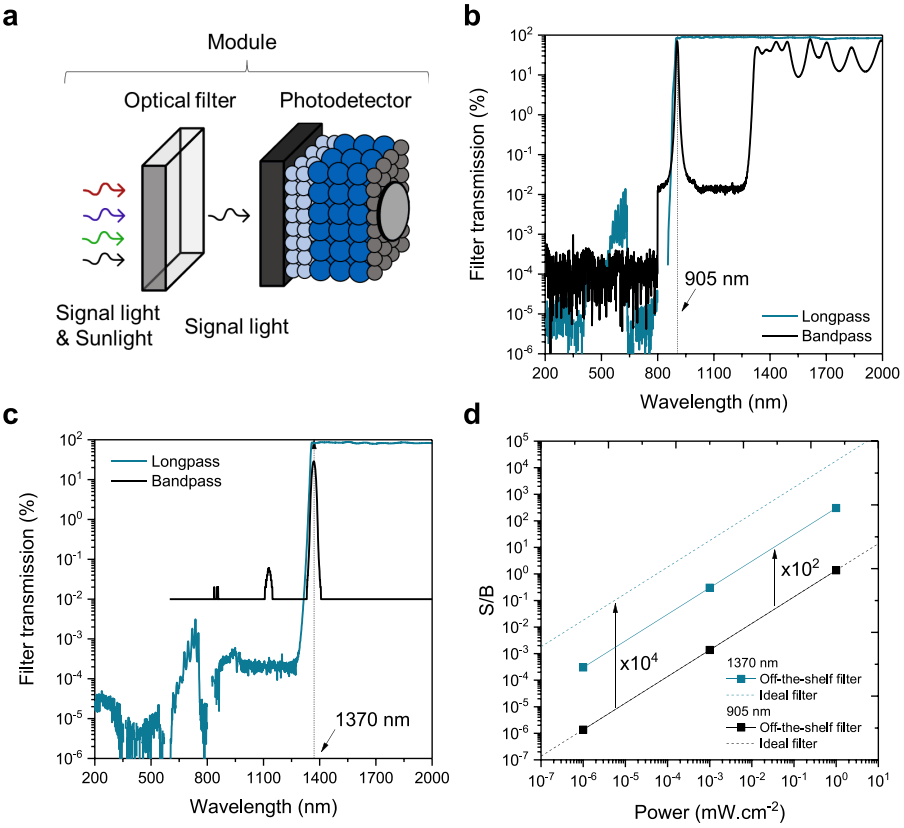

Figure 3. Assembly of photodetector modules. (a) Schematic of a photodetector module: the combination of optical filters with a photodetector. (b) Filters used for the Si-based modules operating at 905 nm. (c) Filters used for the CQD-based modules operating at 1370 nm. d) Estimated S/B (calculated using an idealized filter vs the commercial filters of panels b and c) for operation at 905 and 1370 nm.

based photodetectors operating at 905 nm and measure a 2 orders of magnitude improvement in the signal-to-background ratio (S/B) in the presence of solar radiation.

We fabricated inverted devices using strategies that have been reported in large bandgap CQD ($E_g \sim 1.3$ eV, with excitonic peak at approximately 950 nm). These strategies utilize metal oxides as the electron transport layer (ETL) and a layer of ethane-1,2-dithiol (EDT) treated PbS CQD ($E_g \sim 1.3$ eV) as the HTL. A halide-passivated small bandgap CQD absorber layer ($E_g \sim 0.9$ eV, with excitonic peak at 1370 nm) is placed between the HTL and ETL to complete a PIN (p-doped HTL, intrinsic absorber, and n-doped ETL) architecture. We found that translating these strategies to a 1370 nm operating inverted architecture leads to minimal light response (data in Figure S1), which we attribute to electron extraction barriers at the CQD-ETL interface.

We sought a CQD-based ETL to address the difficulties in fabricating inverted photodetectors operating at 1370 nm. Compared to metal oxides, CQD layers have tunable band edge positions enabled by quantum dot size tuning and surface ligand modification.[20] We sought a surface ligand that would provide the CQD layer with the band alignment and doping required for charge extraction. We pursued a CQD ligand passivation and deposition strategy compatible with the bottom CQD layers (absorber and HTL) to avoid degradation.

Tetrabutylammonium iodide (TBAI) passivated CQD have been demonstrated as a large bandgap absorber layer.[21,22] We found that this strategy did not translate to small bandgap CQD solids (Figures S3 and S4), but we did assess the potential of TBAI-passivated CQD as photodetector ETLs. TBAI provides n-type doping and increases the electron affinity of the layer,[20,23,24] making it potentially suitable for electron extraction. Furthermore, the ligand is exchanged through solid-state methods using ethanol. This process does not damage the underlying absorber CQD layer, ensuring the orthogonality of this process.

The ligand and quantum-size tuning of each layer provided suitable band alignment for carrier extraction (Figures 2a and S5). The CQD devices showed a low dark current at 1 V reverse bias ($\sim 10^{-3}$ mA cm^{-2}) and a rectification ratio of $\sim 10^3$ (Figures 2b and S6). Power-dependent current−voltage (I−V) was measured using an excitation wavelength of 1310 nm (Figure 2b). The photodetectors have an external quantum efficiency of up to 75% (at 1 V reverse bias) at the well-defined excitonic peak of 1370 nm (Figures 2c and S6). Figure 2d shows the dependence of photoresponse on input power.

Photodetection speed was characterized based on the fall-time (90%−10%) which averaged 600 ns (Figure 2e). We observe an improvement in photodetection speed with decreasing area, suggesting that response time for larger pixels (0.049 cm^2) is limited by the device's capacitance (Figure S7).

We characterized the photodetector noise under various operating frequencies. Under short-circuit conditions, the noise current gradually decreases with increasing operation frequency (Figure 2f). This behavior—typical of flicker ($1/f$) noise—has been reported for CQD-based photodetectors.[25,26] We measured a specific detectivity (based on noise current) reaching 7×10^{11} Jones at the excitonic peak (60−100 kHz). Furthermore, the inverted CQD devices have improved EQE and dark current compared to prior literature (using standard,

https://doi.org/10.1021/acs.nanolett.2c02756
Nano Lett. XXXX, XXX, XXX−XXX

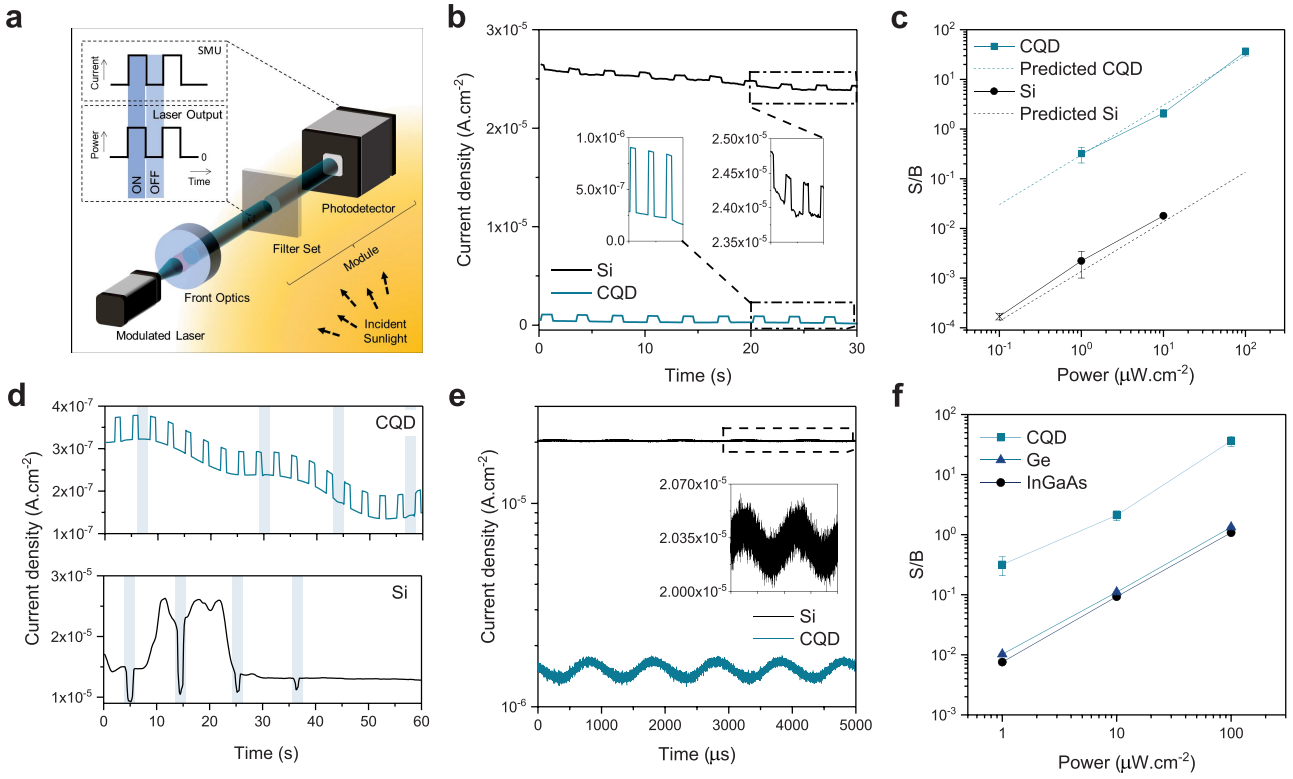

Figure 4. Outdoor performance of the CQD-based module (1370 nm) and silicon-based reference-case detector module (905 nm). (a) Schematic of the outdoor experiment. (b) Output current of modules. (c) S/B of modules. (d) Impact of people moving in the surrounding of the photodetector in module's output current. The blue-highlighted area shows the passage of a person. (e) Higher-speed (1 kHz) measurement. (f) S/B at 1370 nm of CQD-based, Ge-based, and InGaAs-based devices.

inverted and Schottky architectures) in the SWIR (Figure S8). We attribute the improvements in EQE and dark current to improved control over the band alignment enabled by quantum dot size tuning and surface ligand modification. This strategy avoids barriers to carrier extraction. Simultaneously, the large bandgap (~1.3 eV) HTL and ETL layers act as a carrier blocking layer for electrons and holes, decreasing dark current.

We constructed two classes of modules comprised of a photodetector and two optical filters (a bandpass and a long-pass filter) (Figure 3a). The additional long-pass filter assures that no visible light is transmitted. One module was constructed to operate at 905 nm using a commercial Si-based photodetector (Thorlabs DET10A2) and off-the-shelf filters (Thorlabs FEL0900 and FL905−10 Thorlabs; Figure 3b). A second module operates at 1370 nm using the fabricated CQD photodetectors and off-the-shelf filters (Thorlabs FEL1350 and Spectrogon NB-1370-10; Figure 3c). The lower limit of Spectrogon NB-1370-10 measured transmission is limited by the spectrophotometer used, while the transmission of the remaining filters was provided by Thorlabs. As sunlight transmission through the optical filters at 1370 nm is reduced compared to 905 nm, the 1370 nm module is expected to have 2 orders of magnitude higher signal-to-background ratio than the 905 nm module (Figure 3d). We define S/B as the ratio of photocurrent produced by excitation light (I_{signal}) to the photocurrent produced by background sunlight (I_{bg}), using the formula: $S/B = (I_{signal} - I_{bg})/I_{bg}$ (Note S1). We use S/B as the figure of merit as it takes account both device responsivity and optical losses from filters.

To test the performance advantage of CQD-based photodetectors operating at 1370 nm over Si-based photodetectors operating at 905 nm, we devised a field test (Figure 4a). The Si-based and CQD-based modules were tested outdoors, under solar irradiation, using laser light wavelengths of 905 and 1370 nm. The laser light was modulated using pulsed (ON−OFF) square waves. We monitor the signal (laser ON) and background (background current at OFF, which includes a component arising due to solar irradiance in the relevant band) and determined the signal-to-background ratio. The current output of both modules is shown in Figure 4b for a light intensity of 10 μW cm^{-2} (device response under dark conditions is provided in Figures S12 and S13). The current during OFF cycles—dominated by response to solar irradiance—is approximately 100 times higher for the Si module compared to the CQD module. The S/B at three different power densities is around 2 orders of magnitude higher for the CQD module compared to the Si (Figure 4c). The observed improvement matches the predicted values well for the set of filters used (Figure 4c and Note S1).

We observed that the dark current output (OFF cycles) is not constant as the module response is affected by its surroundings—in particular, the movement of clouds and passage of vehicles and people. Figure S17 shows the background current variability (normalized to signal) of both modules. Even though the variability to the average background current (the percent deviation from the average value) is the same for both modules, the absolute background current variation for the same signal level is considerably higher for the Si module. People moving in the surroundings of the photodetector produce large dips in the output current of

https://doi.org/10.1021/acs.nanolett.2c02756
Nano Lett. XXXX, XXX, XXX−XXX

the Si compared to the CQD module (Figure 4d). This further demonstrates the benefit of CQD-based 1370 nm modules compared to Si-based 905 nm modules, as the background current caused by solar irradiance cannot be treated as a constant DC source as it is dependent on the photodetector surroundings.

We evaluated the modules at higher operational frequencies (1 kHz) using laser illumination with a continuous-wave background and a small signal modulation on top (Figure S18). The background component (as seen by the average current) is higher for the Si-based module compared to the CQD-based module (Figure 4e).

We then investigated the performance of photodetectors based on state-of-the-art epitaxial semiconductors—a germanium-based (Ge, Thorlabs SM05PD6A) and InGaAs-based (Thorlabs DET20C2) photodetector—operating at 1370 nm using the same filter system used for the CQD modules (Figure 4f). Even though their S/B is superior to the Si-based module by approximately 1 order of magnitude, the performance is inferior to that of the CQD-based modules. This is due to the transmission of SWIR light (above 1400 nm) through the bandpass filter (optical density of approximately 3 in the 1400−3200 nm spectral range), as shown in Figure S19. As the bandgap of the CQD is tuned to absorb 1370 nm light the most, the responsivity of the CQD-based photodetector drops significantly above 1400 nm acting as a natural built-in filter. This ensures that sunlight above 1400 nm does not contribute to background current as it does for the Ge-based and InGaAs-based modules whose responsivity remains high above 1400 nm. The responsivity tunability associated with CQD-based technologies allows for the use of simpler optical filters compared to Ge-based and InGaAs-based photodetectors. Furthermore, the epitaxial manufacturing associated with Ge and InGaAs requires ultrahigh vacuum and elevated temperatures, elevating module cost and precluding their incorporation in consumer electronics.[10,27]

We fabricated a 1370 nm-operating CQD-based photodetector and demonstrated lower sunlight interference compared to Si-based technologies. We opted for an inverted device architecture, which has demonstrated advantages to the standard (not inverted) structure but remains underexplored. We devised an all-CQD photodetector structure where the surface chemistry of the different CQD layers is tuned to enhance band alignment and achieve low dark current (10^{-3} mA cm^{-2} @ 1 V) and high EQE (~75% @ 1 V). We demonstrated practically the S/B improvement of a CQD module compared to a Si module ($\times 10^2$). The improvement in S/B has the prospect of enhancing imaging capabilities while decreasing power consumption in consumer electronic devices.

■ ASSOCIATED CONTENT

Supporting Information

The Supporting Information is available free of charge at https://pubs.acs.org/doi/10.1021/acs.nanolett.2c02756.

Methods and experimental details; supporting sections including the performance of inverted devices using conventional ETLs; UPS; device performance statistics; large-area pixel transient response and capacitance; comparison with prior CQD literature in the SWIR; filter systems; photodetectors response in dark conditions; representative current−time scans used for outdoor S/B calculation; and experimental methods used for outdoor experiments (PDF)

■ AUTHOR INFORMATION

Corresponding Author

Edward H. Sargent − *Department of Electrical and Computer Engineering, University of Toronto, Toronto, Ontario M5S 3G4, Canada;* orcid.org/0000-0003-0396-6495; Email: ted.sargent@utoronto.ca

Authors

Joao M. Pina − *Department of Electrical and Computer Engineering, University of Toronto, Toronto, Ontario M5S 3G4, Canada;* orcid.org/0000-0002-3448-0028

Maral Vafaie − *Department of Electrical and Computer Engineering, University of Toronto, Toronto, Ontario M5S 3G4, Canada;* orcid.org/0000-0001-9119-6499

Darshan H. Parmar − *Department of Electrical and Computer Engineering, University of Toronto, Toronto, Ontario M5S 3G4, Canada*

Ozan Atan − *Department of Electrical and Computer Engineering, University of Toronto, Toronto, Ontario M5S 3G4, Canada*

Pan Xia − *Department of Electrical and Computer Engineering, University of Toronto, Toronto, Ontario M5S 3G4, Canada*

Yangning Zhang − *Department of Electrical and Computer Engineering, University of Toronto, Toronto, Ontario M5S 3G4, Canada*

Amin M. Najarian − *Department of Electrical and Computer Engineering, University of Toronto, Toronto, Ontario M5S 3G4, Canada*

F. Pelayo García de Arquer − *Department of Electrical and Computer Engineering, University of Toronto, Toronto, Ontario M5S 3G4, Canada; ICFO−Institut de Ciències Fotòniques, The Barcelona Institute of Science and Technology, Barcelona 08860, Spain;* orcid.org/0000-0003-2422-6234

Sjoerd Hoogland − *Department of Electrical and Computer Engineering, University of Toronto, Toronto, Ontario M5S 3G4, Canada;* orcid.org/0000-0002-3099-585X

Complete contact information is available at: https://pubs.acs.org/10.1021/acs.nanolett.2c02756

Funding

This work was supported by the Natural Sciences and Engineering Research Council of Canada (RGPIN-2017-06477).

Notes

The authors declare no competing financial interest.

■ REFERENCES

(1) Gupta, M.; Yin, Q.; Nayar, S. Structured light in sunlight. *Proceedings of the IEEE International Conference on Computer Vision* **2013**, 545−552.

(2) Thorstensen, J.; Tschudi, J.; Haugholt, K.; Bouquet, G.; Kirkhus, T. Structured light imaging under sunlight conditions. *3D Image Acquisition and Display: Technology, Perception and Applications* **2018**, 3M3G-3.

(3) Kazmi, W.; Foix, S.; Alenya, G. Plant leaf imaging using time of flight camera under sunlight, shadow and room conditions. *IEEE International Symposium on Robotic and Sensors Environments Proceedings* **2012**, 192−197, DOI: 10.1109/ROSE.2012.6402615.

(4) Sun, W.; Hu, Y.; MacDonnell, D.; Weimer, C.; Baize, R. Technique to separate lidar signal and sunlight. *Opt. Express* **2016**, *24* (12), 12949−12954.
(5) Padilla, D.; Davidson, P.; Carlson, J.; Novick, D. *Advancements in Sensing and Perception Using Structured Lighting Techniques: An LDRD Final Report*; Sandia National Lab Report: Albuquerque, NM, 2005.
(6) Hadji, B. Understanding Wavelength Choice in LiDAR Systems. *Embedded*, 25 June 2021. https://www.embedded.com/understanding-wavelength-choice-in-lidar-systems/.
(7) O'Sullivan, P.; Dortz, N. Time of Flight. *Analog Devices* **2021**, *55*, No. 3.
(8) Houghton, J. *The Physics of Atmospheres*; Cambridge University Press: New York, U.S.A., 1977.
(9) Wojtanowski, J.; Zygmunt, M.; Kaszczuk, M.; Mierczyk, Z.; Muzal, M. Comparison of 905 and 1550 nm semiconductor laser rangefinders' performance deterioration due to adverse environmental conditions. *Opto-Electronics Review* **2014**, *22* (3), 183−190.
(10) Goossens, S.; Konstantatos, G.; Oikonomou, A. Colloidal Quantum Dot Image Sensors: Technology and Marketplace Opportunities. *Frontline Technology* **2021**, *37* (6), 18−23.
(11) Clifford, J.; Konstantatos, G.; Johnston, K.; Hoogland, S.; Levina, L.; Sargent, E. Fast, sensitive and spectrally tuneable colloidal-quantum-dot photodetectors. *Nature Nanotechnol.* **2009**, *4* (1), 40−44.
(12) Xiao, X.; Xu, K.; Yin, M.; Qiu, Y.; Zhou, W.; Zheng, L.; Cheng, X.; Yu, Y.; Ning, Z. High quality silicon: colloidal quantum dot heterojunction based infrared photodetector. *Appl. Phys. Lett.* **2020**, *116* (10), 101102.
(13) Vafaie, M.; Fan, J. Z.; Morteza Najarian, A.; Ouellette, O.; Sagar, L. K.; Bertens, K.; Sun, B.; Garcia de Arquer, F. P.; Sargent, E. H. Colloidal quantum dot photodetectors with 10-ns response time and 80% quantum efficiency at 1,550 nm. *Matter* **2021**, *4* (3), 1042−1053.
(14) Biondi, M.; Choi, M.-J.; Wang, Z.; Wei, M.; Lee, S.; Choubisa, H.; Sagar, L. K.; Sun, B.; Baek, S.-W.; Chen, B.; Todorovic, P.; Najarian, A. M.; Sedighian Rasouli, A.; Nam, D.-H.; Vafaie, M.; Li, Y. C.; Bertens, K.; Hoogland, S.; Voznyy, O.; García de Arquer, F. P.; Sargent, E. H. "Facet-Oriented Coupling Enables Fast and Sensitive Colloidal Quantum Dot Photodetectors,". *Adv. Mater.* **2021**, *33* (33), 2101056.
(15) Pejović, V.; Lee, J.; Georgitzikis, E.; Li, Y.; Kim, J.; Lieberman, I.; Malinowski, P.; Heremans, P.; Cheyns, D. Thin-Film Photodetector Optimization for High-Performance Short-Wavelength Infrared Imaging. *IEEE Electron Device Lett.* **2021**, *42* (8), 1196−1199.
(16) Kim, J.; Pejović, V.; Georgitzikis, E.; Li, Y.; Kim, J.; Malinowski, P.; Lieberman, I.; Cheyns, D.; Heremans, P.; Lee, J. Detailed Characterization of Short-Wave Infrared Colloidal Quantum Dot Image Sensors. *IEEE Trans. Electron Devices* **2022**, *69* (6), 2900.
(17) Xu, K.; Xiao, X.; Zhou, W.; Jiang, X.; Wei, Q.; Chen, H.; Deng, Z.; Huang, J.; Chen, B.; Ning, Z. Inverted Si: PbS colloidal quantum dot heterojunction-based infrared photodetector. *ACS Appl. Mater. Interfaces* **2020**, *12* (13), 15414−15421.
(18) Dong, C.; Liu, S.; Barange, N.; Lee, J.; Pardue, T.; Yi, X.; Yin, S.; So, F. Long-wavelength lead sulfide quantum dots sensing up to 2600 nm for short-wavelength infrared photodetectors. *ACS Appl. Mater. Interfaces* **2019**, *11* (47), 44451−44457.
(19) Zhang, B. Solution-Processed Broadband Bulk Heterojunction Perovskite Photodetectors. Dissertation, University of Akron, Akron, 2019.
(20) Brown, P.; Kim, D.; Lunt, R.; Zhao, N.; Bawendi, M.; Grossman, J.; Bulovic, V. Energy level modification in lead sulfide quantum dot thin films through ligand exchange. *ACS Nano* **2014**, *8* (6), 5863−5872.
(21) Chuang, C.; Brown, P.; Bulović, V.; Bawendi, M. Improved performance and stability in quantum dot solar cells through band alignment engineering. *Nature materials* **2014**, *13* (8), 796−801.
(22) Xu, Q.; Meng, L.; Sinha, K.; Chowdhury, F.; Hu, J.; Wang, X. Ultrafast colloidal quantum dot infrared photodiode. *ACS Photonics* **2020**, *7* (5), 1297−1303.
(23) Tom, A.; Thomas, A.; Ison, V. Novel post-synthesis purification strategies and the ligand exchange processes in simplifying the fabrication of PbS quantum dot solar cells. *RSC Adv.* **2020**, *10* (51), 30707−30715.
(24) Lan, X.; Voznyy, O.; Kiani, A.; García de Arquer, F.; Abbas, A.; Kim, G.; Liu, M.; Yang, Z.; Walters, G.; Xu, J.; Yuan, M.; Ning, Z.; Fan, F.; Kanjanaboos, P.; Kramer, I.; Zhitomirsky, D.; Lee, P.; Perelgut, A.; Hoogland, S.; Sargent, E. Passivation using molecular halides increases quantum dot solar cell performance. *Adv. Mater.* **2016**, *28* (2), 299−304.
(25) García de Arquer, F.; Gong, X.; Sabatini, R.; Liu, M.; Kim, G.; Sutherland, B.; Voznyy, O.; Xu, J.; Pang, Y.; Hoogland, S.; Sinton, D.; Sargent, E. Field-emission from quantum-dot-in-perovskite solids. *Nat. Commun.* **2017**, *8* (1), 14757.
(26) Liu, H.; Lhuillier, E.; Guyot-Sionnest, P. 1/f noise in semiconductor and metal nanocrystal solids. *J. Appl. Phys.* **2014**, *115* (15), 154309.
(27) Konstantatos, G.; Sargent, E. Solution-Processed Quantum Dot Photodetectors. *Proceedings of the IEEE* **2009**, *97* (10), 1666−1683.

https://doi.org/10.1021/acs.nanolett.2c02756
Nano Lett. XXXX, XXX, XXX−XXX